Sequence-dependent catalysis and assembly to form peptide/Au nanoenzyme for glucose and plasma GSH detecting in cancer patients

Shengtao Wang [a,b,c,1], Anhe Wang [a,b,1], Jingtao Li [d], Qingquan Han [a,b], Yafeng Jing [a,b], Jieling Li [a,b], Shiyu Du [d], Peter H. Seeberger [e,*], Jian Yin [c,*], Shuo Bai [a,b,*]

[a] State Key Laboratory of Biochemical Engineering, Institute of Process Engineering, Chinese Academy of Sciences, Beijing, 100190, PR China
[b] Key Laboratory of Biopharmaceutical Preparation and Delivery, Chinese Academy of Sciences, Beijing, 100190, PR China
[c] Key Laboratory of Carbohydrate Chemistry and Biotechnology, Ministry of Education, School of Biotechnology, Jiangnan University, Wuxi, 214122, PR China
[d] Department of Gastroenterology, China-Japan Friendship Hospital, Beijing, 100029, PR China
[e] Department of Biomolecular Systems, Max Planck Institute of Colloids and Interfaces, Am Mühlenberg 1, Potsdam, 14476, Germany

ARTICLE INFO

ABSTRACT

Metal ions play a pivotal role in regulating and determining the functions of proteins and peptides in nature. This study aims to investigate the regulatory role of metal ions in peptide assembly and explore the influence of sequence variations and metal ions on the structure and function of resulting peptide nanoarchitectures. Dipeptide sequences with distinct charged properties (positive and negative) and functional groups (-COOH, -NH$_2$, and phenolic hydroxyl) were meticulously selected and co-assembled with various metal ions (Au^{3+}, Ag$^+$, and Pt^{4+}). The findings highlight the crucial functional role of the phenolic hydroxyl group of tyrosine in metal ion reduction, while positively charged groups promote metal ion accumulation through electrostatic forces, facilitating co-assembly. The formation of ordered structures in Au@Fmoc-YK and Au@Fmoc-YR nanoarchitectures further validates the significant interaction among metal ions, tyrosine-OH, and positively charged NH$_2$. Notably, these nanoarchitectures possess the unique attribute of being prepared under physiological conditions, specifically at 37 °C, without the need for organic solvents or chemical modifications of peptides. This approach offers a straightforward means of constructing diverse functional nanoarchitectures based on peptides and metal ions. Moreover, Au@Fmoc-YR exhibits good performance as a nanoenzyme for detecting glucose in complex bodily fluids and plasma GSH in tumor patients, showcasing its promising potential for medical applications.

Introduction

In many biological processes, metal ions are essential and play vital roles, and are indispensable for the functionality of natural biomolecules, where metal ions can form stable structures with various functional groups in the biomolecules chain through coordination interactions. This interaction is important in various biological phenomena, including the facilitation of enzyme-catalyzed reactions, maintenance of protein structure and stability, and assistance in DNA replication, RNA transcription, and protein translation [1–4]. Additionally, metal ions have been identified as significant contributors to signaling pathways and immune responses [3,5–10]. Overall, metal ions are integral components of numerous biological systems, and

comprehending their interactions with biomolecules constitutes a crucial area of research [11–13]. Short peptides, as amino acid sequence-encoded building blocks, are a prominent class of biomolecules capable of facilitating supramolecular assembly [14]. Through non-covalent forces such as electrostatic interactions, hydrogen bonding, π-π stacking, and hydrophobic interactions, these peptides can achieve precisely controlled shapes and functions. This assembly process is governed by both thermodynamic and dynamic mechanisms. Consequently, short peptides hold immense potential for a wide range of applications in biomedicine, bio-nanotechnology, and bio-catalysis [15–19]. The assembly behavior of short peptides is influenced by various factors, including pH, temperature, solvent, matrix interface, and guest molecules, especially metal ions [20]. Peptides,

---

characterized by diverse functional groups such as sulfhydryl, indole, amino, and phenolic hydroxyl, have been extensively studied for their interactions with different types of metal ions [21,22] (e.g., Au^{3+} and Ag^+). These interactions have been utilized in the preparation of organic-inorganic hybrid nanomaterials endowed with special functionalities. For example, Rosi's group [23–26] has designed and prepared a range of 1D and 2D superstructures including gold nanoparticle double helices, single-helical gold nanoparticle superstructures and hollow spherical gold nanoparticle superstructures. These structures are created through the redox reaction between tyrosine (Y) of dodecapeptide (AYSSGAPPMPPF) and $HAuCl_4$ in the HEPES solution. Similarly, Metrangolo's group [27] has prepared spherical and chiroptical helical superstructures decorated with Au nanoparticles, relying on the redox reaction between NH_2 of pentapeptide (DFNKF or KLVFF) and $HAuCl_4$ with the help of halogen (I^- or Cl^-) in water at 60 °C. Moreover, Yang's group [28] has demonstrated that NH_2 groups of dipeptides (FF) can interact and reduce Au^{3+} to form dipeptide-gold nanoparticle hybrid spheres in an aqueous solution at 60 °C. In close recent, tyrosine (Y) has been used to prepare high-aspect-ratio gold microwires (>500) in 2 M NaCl aqueous solution at 80 °C [29]. Although many novel and unique superstructures based on peptides and metal ions have been reported, the preparation process for forming hybrid peptides and metal ion nanoarchitectures still requires harsh conditions, including high temperatures, excess reducing agents, and complex procedures. Furthermore, there is still a lack of understanding about the regulation of peptide assembly by metal ions, as well as the effect of peptide sequence and metal ions on the structure and function of formed peptide nano-architectures. These challenges underscore the need for further research in this field to develop new synthesis methods for hybrid peptide and metal ion nanoarchitectures with improved properties while minimizing complexity.

Herein, a series of dipeptides with different positive and negative charges and functional groups including Fmoc-YA, Fmoc-YD, Fmoc-YK, Fmoc-YL, Fmoc-YR, and Fmoc-YW were designed to investigate the specific role of different peptide functional groups in their interaction with various metal ions (Au^{3+}, Ag^+ and Pt^{4+}) to form hybrid nano-architectures under a mild condition (neither elevated temperatures nor reducing agents or chemical modification of peptides are required). This research aims to provide a comprehensive understanding of the molecular mechanisms involved in the formation of hybrid materials and may have important implications for the development of new strategies for designing nanomaterials with unique properties for various applications. As a proof of concept, the formed hybrid Au@Fmoc-YK and Au@Fmoc-YR NPs were found to have good conductivity and catalysis performance, which were further employed in the detection of glucose using a straightforward electrochemical method [30] (Scheme 1). In addition, Au@Fmoc-YR assemblies were used to detect plasma GSH content in tumor sites of patients with gastric carcinoma, which was much higher than that of healthy adults (3.39 ± 1.04 μM) [31], showing good potential application as early, metastatic, and recurrent cancers screening tool.

Experimental section

Materials

Chloroauric acid ($HAuCl_4 \bullet 4H_2O$) (99.9%) was purchased from Sinopharm Chemical Reagent Co., Ltd (China). Nafion (5 wt%) and L-Glutathione reduced were purchased from Sigma-Aldrich. Sodium borohydride was purchased from Shanghai Aladdin Bio-Chem Technology Co., Ltd (China). Fmoc-YK (98%), Fmoc-YA (98%), Fmoc-YD (98%), Fmoc-YL (98%), Fmoc-YR (98%), YK (98%), Fmoc-Y (98%), Fmoc-Y-OMe (98%), Fmoc-K (98%) and Fmoc-K-OMe (98%) were purchased from GL Biochem (Shanghai) Ltd (China). Glucose oxidase, 3,3′,5,5′-Tetramethylbenzidine (TMB), glucose, p-nitrophenol, and p-aminophenol were purchased from J&KScientificc Ltd (China). PBS buffer with different pH was purchased from Inner Mongolia Opcel Biotechnology Co., Ltd. All aqueous solutions were prepared using ultrapure water (18.2 MΩ•cm) from the Milli-Q system (Millipore, USA).

Preparation of spherical assemblies of Au@Fmoc-YK and Au@Fmoc-YR

100 μL 10 mM $HAuCl_4$ aqueous solution was mixed with 900 μL different concentrations of Fmoc-YK or Fmoc-YR aqueous solution, and
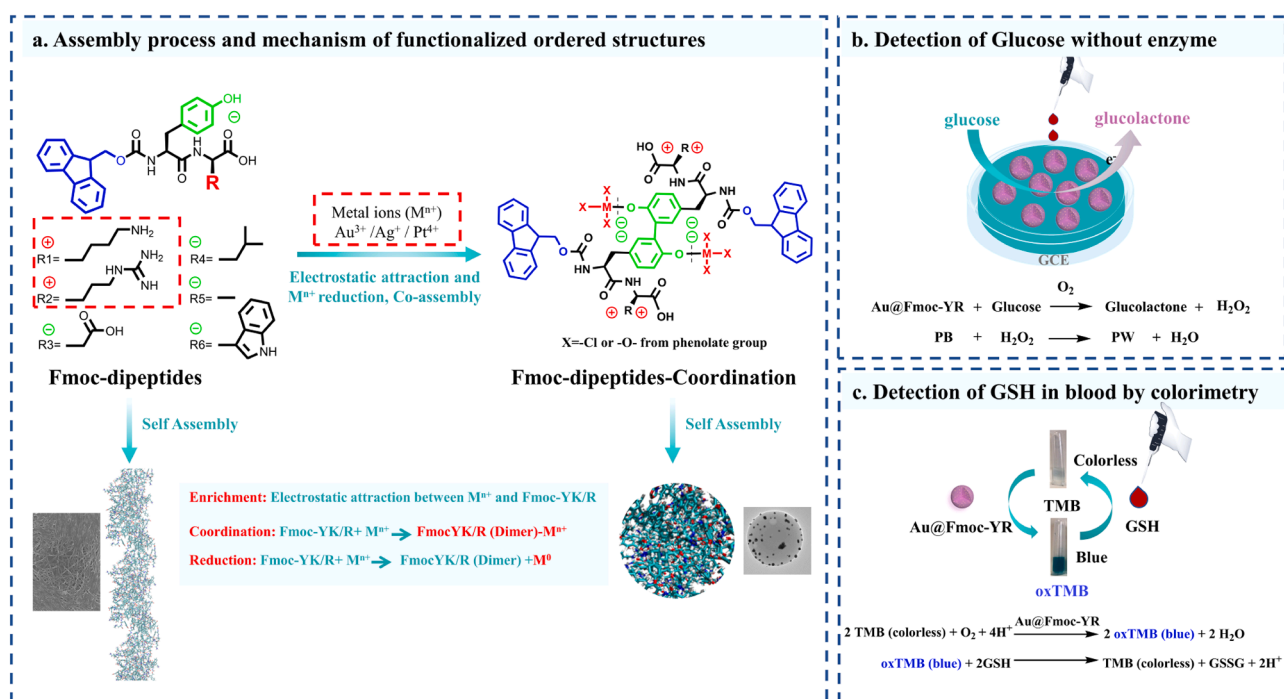
Scheme 1. Schematic illustration of the morphology transformation of assemblies based on dipeptides mediated by metal ions in an aqueous solution at room temperature and its application for glucose and GSH detection.

then the mixing solution was gently shaken for 1 min and then placed for 12 h at room temperature. The monodispersed spherical assemblies of Au@Fmoc-YK or Au@Fmoc-YR were obtained by centrifuging at 10,000 rpm for 5 min and then stored at 4 °C.

Exploration and analysis of factors that affect the formation of spherical assemblies of Au@Fmoc-YK

In common, temperature and concentration had an important influence on the formation of the assembly. In this paper, the temperature was set to 4 °C, 25 °C, 37 °C, 50 °C and 60 °C. The concentration of Fmoc-YK was set to 0.05 mM, 0.1 mM, 0.25 mM, 0.4 mM, 0.5 mM, and 1 mM. All the experiments were performed according to the process described above. The optimal condition: the temperature was set to R.T., the concentration of Fmoc-YK was set to 0.5 mM, and the concentration of $HAuCl_4$ was set to 10 mM.

The characterization of functional spherical assemblies of Au@Fmoc-YK

The open circuit potential of Fmoc-YK solution, $HAuCl_4$ solution, and the mixture solution of Fmoc-YK and $HAuCl_4$ were measured by using a CHI760 electrochemical work station employed with a modified glassy carbon electrode (GCE) as working electrode, a saturated Ag/AgCl electrode as reference electrode and the electrolytic solution was 0.5 M $LiClO_4$ in acetonitrile. 10 μL of the above solution was dropped on the surface of the glassy carbon electrode and dried in the air at room temperature. Then 10 μL of 5 wt% Nafion solution was dropped on the surface of the glassy carbon electrode and dried in the air at room temperature. The open circuit potential of the above solution was obtained from open circuit potential versus the time curve.

Exploration and analysis of the mechanism of the formation of spherical assemblies of Au@Fmoc-YK

Fmoc-YK had an important role in the formation process of spherical assembly Au@Fmoc-YK, in order to determine how did it work, a series of controlled experiments were designed. First, Fmoc-K and Fmoc-K-OMe were chosen and mixed with $HAuCl_4$ in the same condition to determine which amino acid (tyrosine or lysine or both) had redox with $HAuCl_4$. Second, Fmoc-YA, Fmoc-YD, and Fmoc-YL were chosen and mixed with $HAuCl_4$ in the same condition to determine if lysine was necessary and what role lysine played in the formation of spherical assembly Au@Fmoc-YK. Third, Fmoc-YR was chosen to verify the reference about the formation mechanism of the spherical assembly. All the above experiments were performed in the condition accordance with Fmoc-YK.

Detection of glucose

The electrochemical method was often used to detect the concentration of glucose in different samples. The glucose oxidase electrode was prepared according to literature reports [32] and the details were shown in supporting information. The charge transfer coefficient (α) and electron transfer rate constant (ks) were obtained from the linear relationship of peak current (I_p) vs scan rate (υ) and peak current potential (E_p) vs natural logarithm of scan rate ($\ln(\upsilon)$) according to previous researches [33–37]. The surface coverage concentration (Γ^*) of glucose oxidase on GCE/PB/GOx/Au and active surface area of GCE/PB/-GOx/Au (A_{eff}) were calculated by using CVs in 5 mM $K_3[Fe(CN)_6]$ solution of 0.1 M KCl from −0.2 to 0.6 V (versus Ag/AgCl) with the scan rate of 50 mV·s^{-1} according to previous researches [34–36]. The amperometric response experiments were performed in 0.05 M PBS (pH 7.0) with the addition of a different volume of glucose solution or interference solution at an operating potential of −0.05 V.

Results and discussion

Interaction of dipeptides with metal ions in an aqueous solution

Some peptides and proteins with certain functional groups can reduce mental ions to form ordered nanocomposite architectures [27–29,38–41]. Herein, a series of dipeptides (Fmoc-YA, Fmoc-YD, Fmoc-YK, Fmoc-YL, Fmoc-YR, and Fmoc-YW) were synthesized to identify the role of sequences and functional groups of peptides in metal ions reduction (Fig. 1). As described in the experimental section, the color of the mixed aqueous solution changed from light yellow to purple, indicating that Au NPs were formed due to a redox reaction between peptide and Au^{3+}. These peptides (Fig. 1) show different zeta potentials in aqueous solution, for example, Fmoc-YA (−27.6 ± 2.1 mV), Fmoc-YL (−58.9 ± 4.1 mV), Fmoc-YD (−24.7 ± 1.2 mV) and Fmoc-YW (−27.6 ± 2.1 mV) give a negative value due to being rich in carboxyl and phenolic hydroxyl groups in contrast to those of Fmoc-YK (50.7 ± 3.6 mV) and Fmoc-YR (33.6 ± 5.8 mV) with abundant amino groups. The resulting Fmoc-YK and Fmoc-YR dipeptides self-assembled into uniform nanospheres after mixing with $HAuCl_4$ (Fig. 2, Fig. 3a-d and Fig. S1), while Fmoc-YA, Fmoc-YD, Fmoc-YL, and Fmoc-YW formed amorphous structures (Fig. 2). However, we previously demonstrated that Fmoc-YA, Fmoc-YD, Fmoc-YL, Fmoc-YK, and Fmoc-YR could self-assemble into nanofibers through noncovalent interactions in aqueous solution (Fig. 3a,c) [42–44].

To determine, which of the amino, phenolic hydroxyl, and sulfhydryl groups plays the main role in the formation of nanospheres based on dipeptides and $HAuCl_4$, Fmoc-YK and its derivatives (Fmoc-K and Fmoc-K-OMe) were selected to study the effect of different groups. No products were observed in LC-MS when Fmoc-K or Fmoc-K-OMe were mixed with $HAuCl_4$ (Fig. 3e-j), demonstrating that amino and carboxyl groups are unable to reduce $HAuCl_4$ under mild conditions. Di-Fmoc-YK was found after mixing Fmoc-YK with $HAuCl_4$ (Fig. 3i, j and Fig. S2). Moreover, the formation of di-Fmoc-YK was supported by the relatively broad region and peak shift of the aromatic protons in the ^1H NMR spectrum compared with the Fmoc-YK monomer [41,45] (Fig. S3). Therefore, the phenolic hydroxyl group of tyrosine is likely responsible for the electron transfer redox reaction between Fmoc-YK and $HAuCl_4$ to form metal NPs and a phenolic hydroxyl dimer [29] (Fig. S3b).

Fmoc groups have been reported to endow dipeptides with hydrophobic interactions and the ability of self-assembly to form ordered nanoarchitectures [27,28], while amide groups enrich mental ions under the electrostatic attraction [28]. To explore differences of various dipeptides in assembly behavior and study the role of amide and fluorene methoxycarbonyl (Fmoc) groups in the formation of peptide nanospheres, different concentrations of Fmoc-YK, YK, and Fmoc-Y were mixed with $HAuCl_4$ under the same conditions. The SEM images of products (Fig. S4) indicated that YK and Fmoc-Y could not self-assemble into peptide nanospheres, unlike Fmoc-YK. Based on the aftermentioned results, it was supposed that the phenolic hydroxyl served as reductant, and the amide or guanidine groups in Fmoc-YK or Fmoc-YR interacted with $AuCl_4^-$ via electrostatic interactions reducing the electrostatic repulsion between oxidized peptides, thus benefitting peptide self-assembly into nanospheres stabilized Au NPs. We supposed that dipeptide sequences that met the following demands might be able to interact with $HAuCl_4$ to form monodisperse spherical assemblies. First,
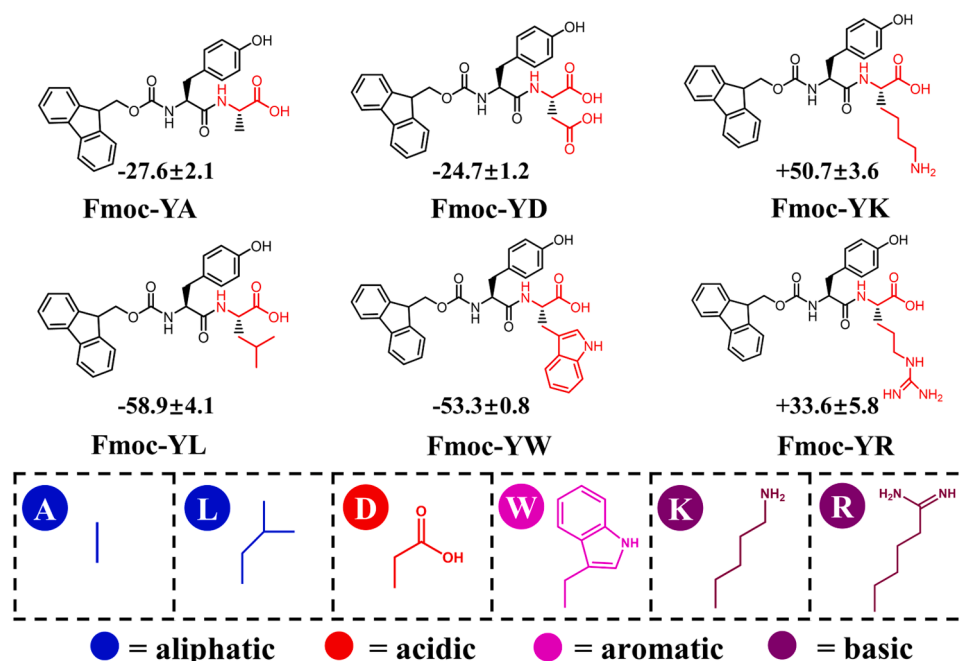
Fig. 1. The physicochemical properties of six kinds of dipeptides.

the dipeptide could self-assemble to form an ordered structure. Second, the dipeptide had a reducing functional group. Third, the dipeptide was positively charged in aqueous solution.

Molecular dynamics simulations (Fig. 4 and **Fig. S5**) revealed the radial distribution function of Fmoc- group, O-Au, and N—Cl$^-$ bonds (Fig. 4a-b) to show that: i) long-range coupling exists between Fmoc groups; ii) Au had strongly correlated with tyrosine OH; iii) Cl$^-$ was strongly correlated with NH$_2$ of tyrosine. The molecular stacking mode between Fmoc-YK and HAuCl$_4$ (**Fig. S5**) also showed that there was a strong coupling between positive NH$_2$ and negative Cl$^-$. It was believed that a long positive side chain wrapping AuCl$_4^-$ was required to form a spherical structure, while other peptides that were not charged or negatively charged could not form a spherical structure. The molecular dynamics simulations further supported the experimental hypothesis aftermentioned.

It was worth noting that Pt@Fmoc-YR nanospheres were obtained under the same condition by mixing Fmoc-YR with H$_2$PtCl$_4$, and Ag@Fmoc-YR nanospheres could be obtained by mixing Fmoc-YR and AgNO$_3$ at 60 °C (**Fig. S6**). The method presented in this study for preparing functionalized ordered assemblies using Fmoc dipeptides and various metal ions demonstrates a certain degree of universality. It contributes to our understanding of the interaction between peptides and metal ions in the formation of ordered functional structures. Additionally, it opens up avenues for the exploration and development of minimalistic catalysts or high-performance materials based on simple peptides with sequence-dependent functionality.

Preparation and characterization of Au@Fmoc-YK and Au@Fmoc-YR

Positively charged peptides (Fmoc-YK and Fmoc-YR) form a uniform and well-dispersed nanospheres containing Au NPs. Gold NPs with a size of about 16.1 ± 3.0 nm ($n = 20$) were observed within nanospheres (**Fig. S7a**). The high-resolution TEM image showed a lattice structure of Au NPs with a lattice distance of about 0.2 nm ascribed to {111} planes of Au NPs [46] (**Fig. S7b**). Moreover, the absorption peak at 540 nm in the UV–Vis spectrum (**Fig. S8**) and EDS element mapping indicated the formation of Au NPs [45] (**Fig. S7c-f**). SEM images displayed good dispersibility and uniformity of Au@Fmoc-YK (**Fig. S9**) with a size of about 245.5 ± 27.2 nm (25 °C). To further investigate the effect of

reaction parameters on the formation of nanocomposites, reaction temperatures were altered. Au@Fmoc-YK of various sizes were obtained at different temperatures, such as 82.6 ± 21.6 nm (4 °C), 245.5 ± 27.2 (25 °C), 89.2 ± 15.3 (37 °C) and 62.5 ± 11.2 nm (60 °C) (**Fig. S9**). At a HAuCl$_4$ concentration, the Au@Fmoc-YK tended to form bigger nanospheres that finally self-assembled into fibers (2 mM) because of excessive amounts of unoxidized Fmoc-YK molecules (**Fig. S10**).

The open circuit potential of Fmoc-YK and HAuCl$_4$ was given with a difference of about 0.2 V, explaining why a higher temperature or addition of reducing agents was not necessary to form uniform and dispersible Au@Fmoc-YK nanospheres (Fig. 5a). FTIR spectra of Fmoc-YK (long nanofibers) and Au@Fmoc-YK (nanospheres) were also observed (Fig. 5b, c). It was found that the stretching vibration of amines (NH) shifted from 3303 cm^{-1} (Fmoc-YK) to 3396 cm^{-1} (Au@Fmoc-YK), which could be ascribed to interaction with Au ions. The corresponding peaks of carboxyl groups (COOH) at 2951 cm^{-1} and 3065 cm^{-1} did change, further demonstrating carboxyl groups didn't participate in redox reaction and interaction with mental ions. In addition, peaks located at 1651 cm^{-1} and 1612 cm^{-1} could be ascribed to α-helix and β-sheet of Fmoc-YK fibers, respectively. However, the signal of those two secondary structures disappeared in the spectrum of Au@Fmoc-YK, strongly suggesting that morphology changes of assemblies from fibers to nanospheres [47,48]. The formation of Au NPs was confirmed by XPS and XRD (Fig. 5d, e). A doublet centered at 84.5 eV and 88.2 eV corresponded to the binding energies of Au 4f$_{7/2}$ and Au 4f$_{5/2}$ of Au^0 and a doublet centered at 86.6 eV and 90.3 eV corresponded to the binding energies of Au 4f$_{7/2}$ and Au 4f$_{5/2}$ of Au$^+$ (Fig. 5d) [46]. Eight well-resolved diffraction peaks were observed for Au@Fmoc-YK and 2θ was 38.16, 44.36, 64.64, 77.62, 81.68, 98.34, 111.04 and 115.22°, which corresponded to the typical face-centered cubic (fcc) Au crystal planes of (111), (200), (220), (311), (222), (400), (331) and (420), respectively [49] (Fig. 5e). The new peak at 258 cm^{-1} in the Raman spectrum might be assigned to the Au-O bond between Au and phenolic hydroxyl of tyrosine which facilitated the formation of nanosphere assemblies [50] (Fig. 5f).

Peptide nanospheres derived from Fmoc-YR were also characterized in detail. Fmoc-YR was self-assembled into fibers in an aqueous solution, similar to Fmoc-YK (Fig. 3a, c). Then, monodisperse nanospheres (denoted as Au@Fmoc-YR) were observed after mixing Fmoc-YR with
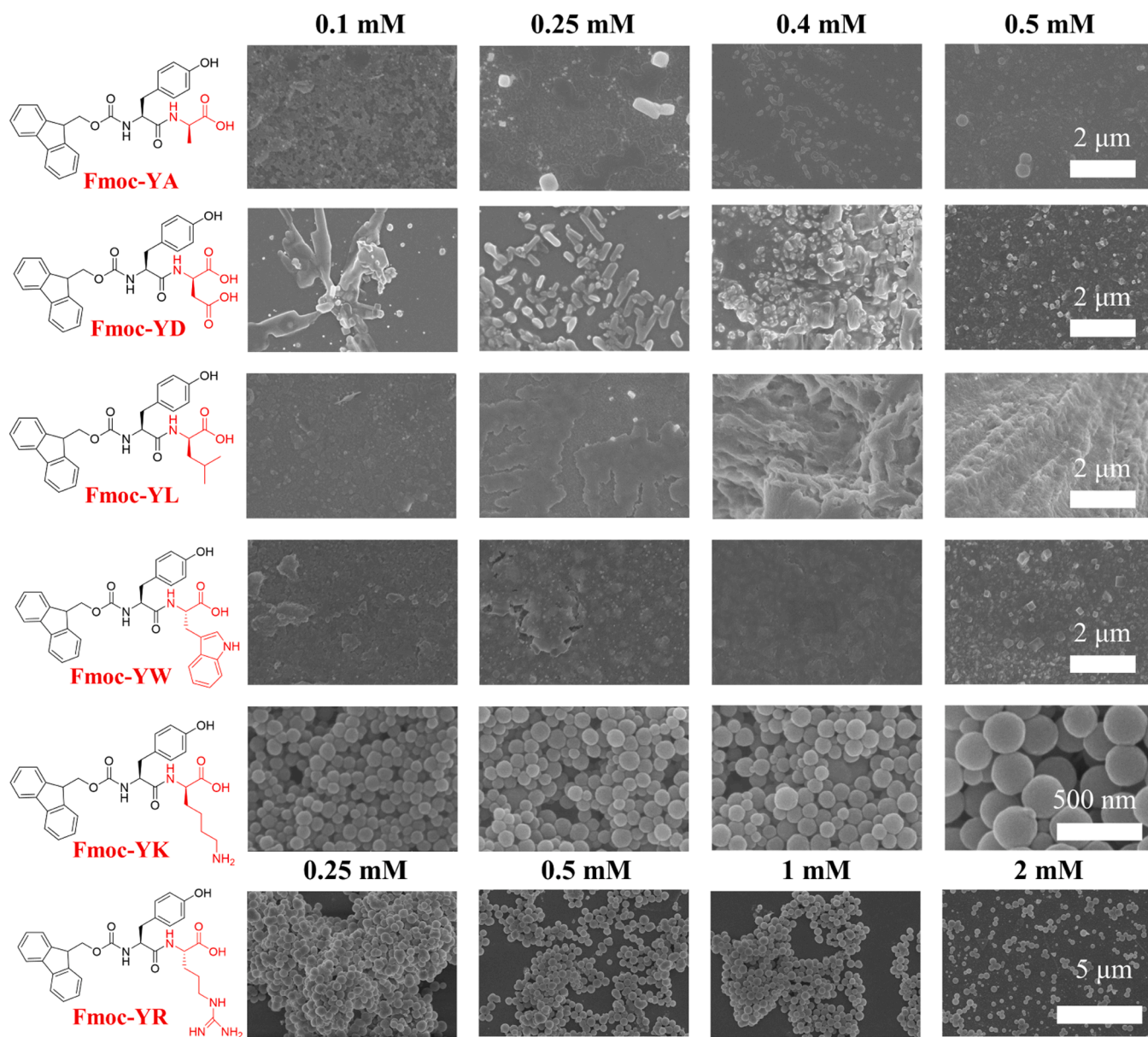
Fig. 2. The SEM images of Fmoc-YA, Fmoc-YD, Fmoc-YL, Fmoc-YW, Fmoc-YK, and Fmoc-YR with different concentrations after incubating with 10 mM HAuCl$_4$ at room temperature.

HAuCl$_4$ (Fig. 2 **and** Fig. 3**a-d**). In the FTIR spectrum of Au@Fmoc-YR, the peak of β-sheet (1625 cm^{-1}) and α-helix (1654 cm^{-1}) disappeared, indicating the morphology changed from nanofibers to nanospheres. Moreover, the stretching vibration peak of amines (NH) and hydroxyl of a carboxyl group (COOH) showed similar behavior to that of Au@Fmoc-YK [47,48] (**Fig. S11a, b**). XRD and XPS spectra confirmed the formation of Au NPs, which was consistent with the results of Au@Fmoc-YK [46,49] (**Fig. S11c, d**). Meanwhile, the ^{1}H NMR of Au@Fmoc-YR had a similar change to that of Au@Fmoc-YK [41,45] (**Fig. S12**). The evolution of Au@Fmoc-YR after the addition of HAuCl$_4$ during 48 h aging (**Fig. S13**), showed that the nanospheres gradually grow and form uniform and dispersible particles with a size of about 200 nm. In particular, Au@Fmoc-YR could be fabricated on a large scale of 15 and 50 mL (**Fig. S14**). Herein, we demonstrated a facile method to prepare order short peptide nanoarchitectures in an aqueous solution at mild conditions. No external reducing agents, high temperature, or a trace amount of organic solvent agent was required compared with other methods [27–29,38–41].

Electrochemical characterization of modified glassy carbon electrode (GCE)

Notably, no reduction peak was observed for the GCE within the range of −0.1 to +0.1 V (Fig. 6**a**). In contrast, both the GCE/PB and GCE/PB/GOx/Au systems exhibited two pairs of redox peaks spanning from −0.4 V to +1.2 V, indicating the successful deposition of the PB film onto the surface of the GCE. The reduction peak at approximately +0.1 V could be ascribed to the reduction peak of H$_2$O$_2$, consistent with earlier results [40].

Cyclic voltammograms (CVs) (Fig. 6**b**) were employed to monitor the electrochemical behavior of GCE and modified GCE. The GCE exhibited no significant current signal (Fig. 6**b**), whereas the GCE modified with Prussian Blue (GCE/PB) displayed a pair of redox current peaks at approximately +0.2 V. The molecular structures of the compounds of PW and PB had been reported previously (**Fig. S15**). Upon immobilizing glucose oxidase (GOx) and Au@Fmoc-YR on the surface of GCE/PB, both the cathodic and anodic peak currents decreased compared with
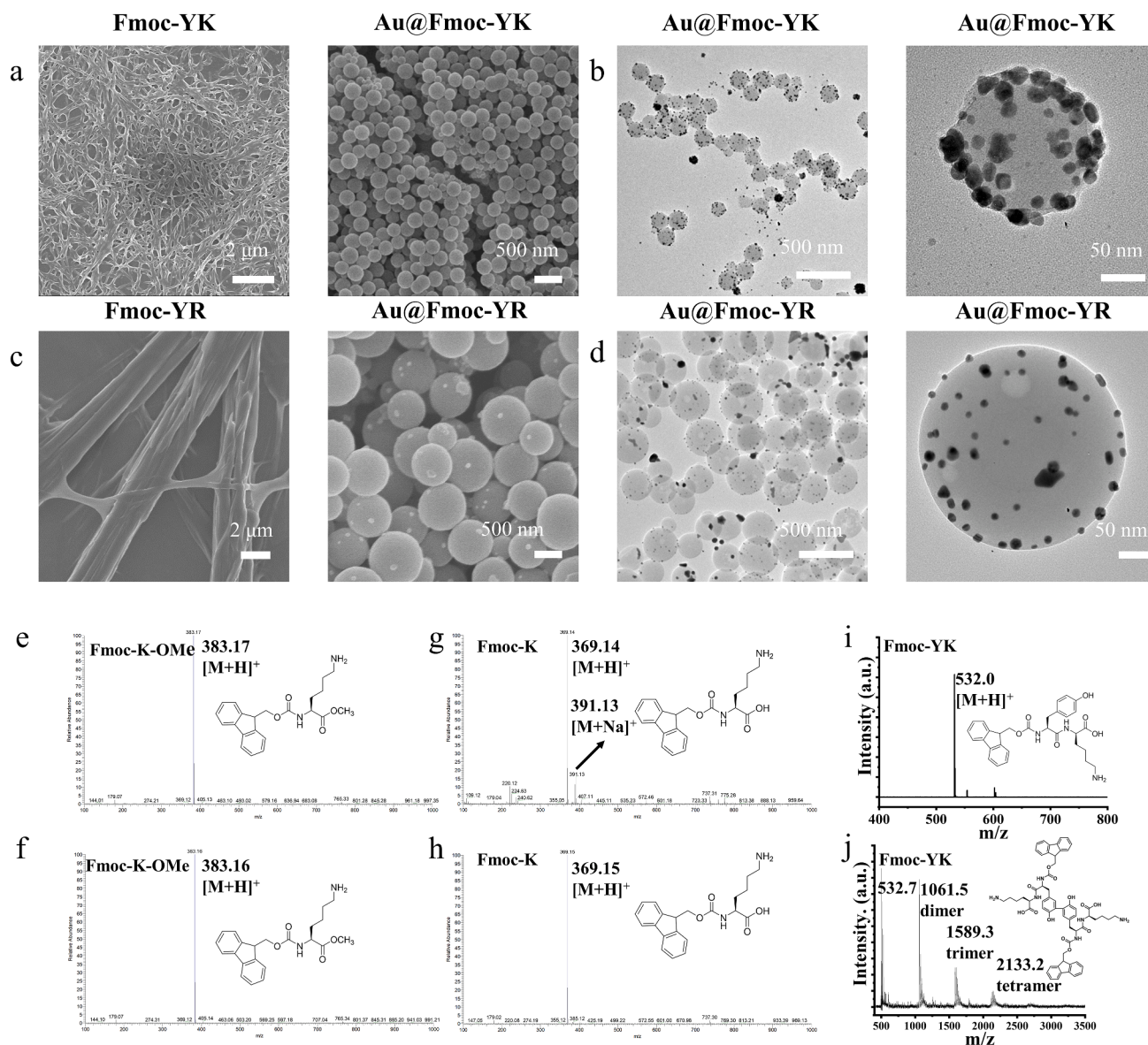
Fig. 3. The morphology and spectral properties changes of Fmoc and Au@Fmoc-YK and the mass spectrometry of different peptides. a) SEM images of Fmoc-YK and Au@ Fmoc-YK. **b)** TEM images of Au@ Fmoc-YK. **c)** SEM images of Fmoc-YR and Au@ Fmoc-YR. **d)** TEM images of Au@ Fmoc-YR. The LC-MS of **e-f)** Fmoc-K-OMe and **g-h)** Fmoc-K and the MALDI-Tof of **i-j)** Fmoc-YK before and after incubation with 10 mM HAuCl$_4$ at room temperature.

that of GCE/PB. This decrease suggests that the presence of the PB film, along with GOx and Au@Fmoc-YR, on the surface of GCE/PB hinders electron transfer [40] (Fig. 6**b**).

The electrochemical impedance spectroscopy (EIS) was further used to value the impendence change of the electrode surface after the modification (Fig. 6**c**). For bare GCE, a typical EIS spectrum consisted of a small semicircle (Ret = 150 Ω) was observed. As the surface of GCE was modified with a PB film and Au@Fmoc-YK alongwith GOx in turn, the Ret value of GCE/PB and GCE/PB/GOx/Au increased to about 300 Ω and 400 Ω, indicating Au@Fmoc-YK and GOx had been successfully immobilized on the surface of GCE/PB.

Quantitative detection of glucose as a biosensor

To assess the performance of GCE/PB/GOx/Au for glucose detection, cyclic voltammograms (CVs) were conducted on GCE/PB with different modifications. Upon the modification of Au@Fmoc-YR on the surface of GCE/PB (GCE/PB/Au), an oxidation peak current of 50 μA was observed, which can be attributed to the excellent conductivity of Au

NPs. This finding was consistent with previous studies [40] (Fig. 6**d**). Conversely, when GCE/PB was modified with GOx (GCE/PB/GOx), the electrode exhibited a higher oxidation peak current compared to GCE/PB/Au, reaching 90 μA. Moreover, when both Au@Fmoc-YR and GOx were deposited on the surface of GCE/PB, a significantly higher oxidation peak current of 135 μA was observed due to the excellent conductivity of the biocompatible Au@Fmoc-YR.

The influence of scan rates on the voltammetric response of glucose was also investigated [32,35]. The CV data of GCE/PB/GOx/Au at various scan rates ranging from 0.01 to 0.3 V·s^{-1} (Fig. 6**e**), revealed that the redox peak currents and peak-to-peak separation increased with increasing scan rate. The linear relationships were established with two linear regression equations as I_{pa} (μA) = 243.85 υ (V·s^{-1}) + 4.44 (R^2 = 0.988) and I_{pc} (μA) = −161.84 υ (V·s^{-1}) - 1.79 (R^2 = 0.997) (Fig. 6**f**). The anodic and cathodic peak potentials were linearly related to the logarithm of scan rates (υ) in the range from 0.18 to 0.3 V·s^{-1} with the slope of 2.3RT/(1-α) nF and −2.3RT/αnF according to Laviron theory [35] (Fig. 6**g**). The charge transfer coefficient (α) was calculated to about 0.599, thus, the electron transfer rate constant (ks) derived from
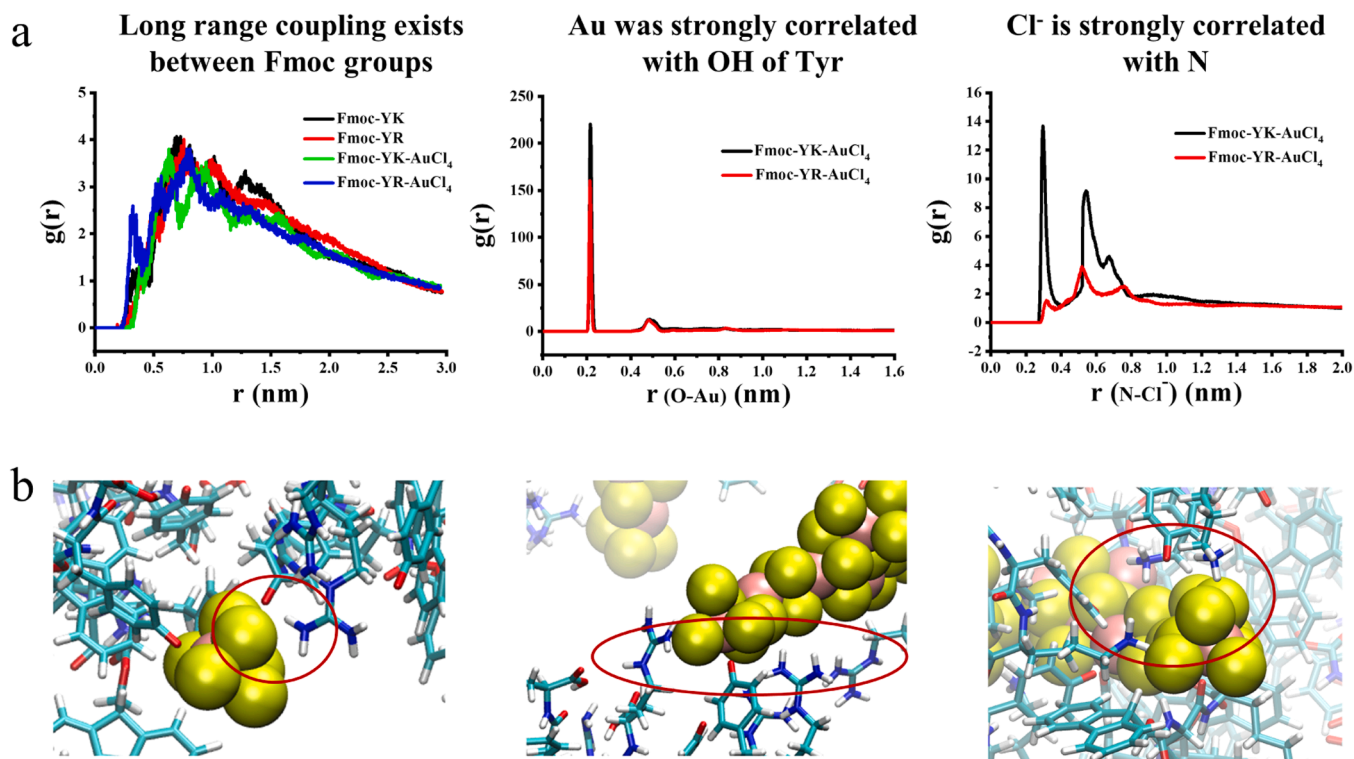
Fig. 4. The results of molecular dynamics simulations. a) The radial distribution function of the group of Fmoc, O-Au, and N—Cl$^-$. **b)** The molecular stacking mode between Fmoc-YK and HAuCl$_4$ in the peptide nanospheres. There is a strong coupling between positive N^+ and negative Cl$^-$. Red O, blue N, green Cl, pink Au.
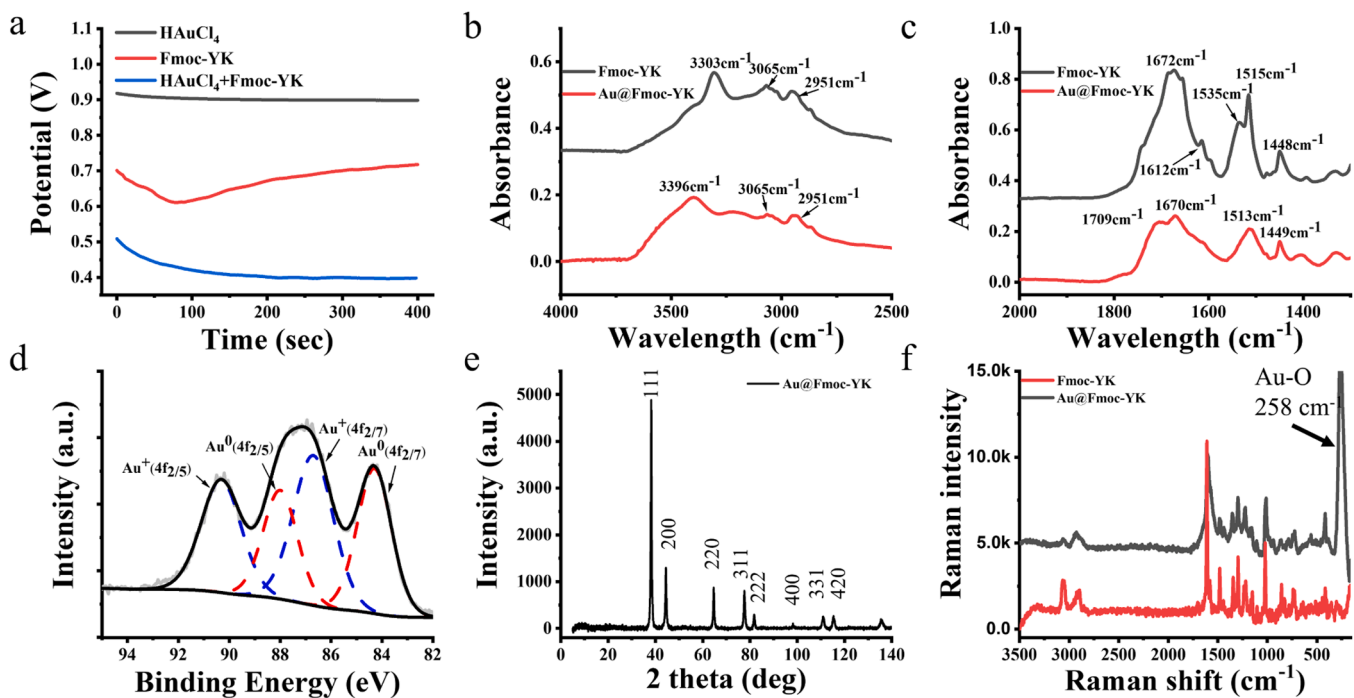
Fig. 5. The spectral properties of Fmoc-YK and Au@Fmoc-YK. a) The open circuit potential of Fmoc-YK, HAuCl$_4$, and the mixture of Fmoc-YK, HAuCl$_4$. **b-c)** The FTIR spectrum of Fmoc-YK and Au@Fmoc-YK. **d)** The XPS spectrum of Au@Fmoc-YK. **e)** The XRD spectrum of Au@Fmoc-YK. **f)** The Raman spectrum of Au@F-moc-YK.
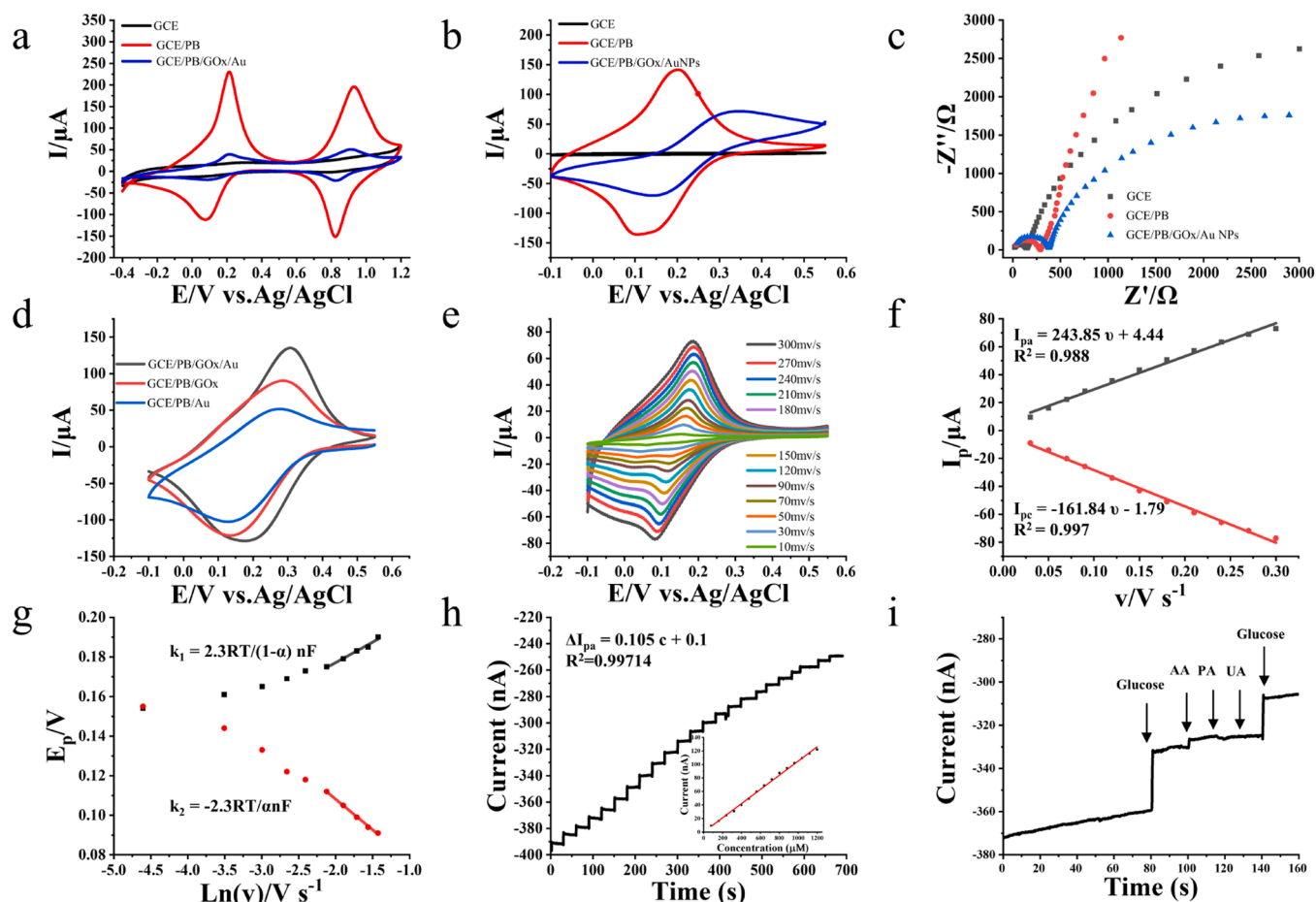
Fig. 6. The electrochemical property of glucose oxidase electrode modified with Au@Fmoc-YK. a) Typical CVs obtained at the bare GCE, PB-modified GCE, and GCE modified with PB and GOx in 0.10 M KCl solution buffered with 0.05 M PBS (pH 7.0), scan rate: 50 mV·s^{-1}. **b)** Cyclic voltammograms at pH 7.0 PBS at GCE, GCE/PB, and GCE/PB/GOx/Au NPs. **c)** Nyquist plots obtained at bare GCE, GCE/PB, and GCE/PB/GOx/Au NPs in 5 mM [Fe(CN)$_6$]$^{3-/4-}$ (1:1). **d)** Cyclic voltammograms obtained at different modified GCEs (AuNPs, GOx, AuNPs+GOx) in 1 mM glucose (pH 7.0 PBS) under ambient air. **e)** Cyclic voltammograms of 1.0×10^{-3} M Glucose in pH 6.8 PBS with different scan rates at GCE/PB/Gox/Au NPs. **f-g)** Linear relationship of (f) I$_p$ vs. υ (υ: 0.03–0.3 V·s) and (g) E$_p$ vs. ln(υ) (υ: 0.18–0.30 V·s); **h-i)** The chronoamperometric responses of the glucose sensors (GCE/PB/GOx/Au) to h) different concentration glucose solutions and i) glucose and different interference in PBS, the inserted graph was the linear relationship between glucose concentration and the change of peak current.

the Laviron equation.

As the scan rate was 0.3 V·s^{-1}, ks was calculated to be 2.08 s^{-1}, While the corresponding value was only about 0.69 s^{-1} for GCE/PB/GOx, indicating Au@Fmoc-YR modification can accelerate the electron transfer rate and improve the detection sensitivity for glucose, which was supported by the higher oxidation peak current in CVs (Fig. 6**d**).

The surface coverage concentration (Γ*) of electroactive GOx at the modified electrode was calculated to be approximately 15.23×10^{-9} mol·cm^{-2} using the equation reported [34,36]. The real active surface area (A) of GCE/PB/GOx/Au was obtained by cyclic voltammetry at 5 mM K$_3$[Fe(CN)$_6$] in 0.1 M KCl solution at a scan rate of 50 mV·s^{-1} based on the equation [36]. The concluded value was higher than the theoretical value of surface coverage concentration (Γ*) (2.86×10^{-12} mol·cm^{-2}) for the monolayer of GOx on a bare electrode surface [61] and other glucose sensors such as GCNT/GOx/GAD composite film on GCE [33] (3.88×10^{-9} mol·cm^{-2}) and GOx-FF-rGO/GCE (2.33×10^{-9} mol·cm^{-2}), indicating the high surface-to-volume ratio and good dispersibility of Au@Fmoc-YR nanospheres facilitated the immobilization

Table 1
Performance comparison of various electrodes modified with GOx for the detection of glucose.

| GOx modified electrodes	E$_{pa}$(V)	Γ*(mol·cm^{-2})	ks (s^{-1})	Liner range	Sensitivity	Detection limit	Ref.
GCE/CNT/Au/PDDA-GOx	−0.3	4.91×10^{-10}	1.01	0.5–5 mM	3.96 mA·M^{-1}·cm^{-2}	–	[51]
GNP/MWCNTs/GOx	−0.2	–	–	up to 9 mM	7.3 µA·mM^{-1}·cm^{-2}	0.128	[52]
GCE/CNT/PTBOGOx	−0.1	–	–	1–7 mM	14.5 mA·mM^{-1}·cm^{-2}	–	[53]
GOx/NdPO$_4$ NPs/CHIT	+0.4	2.95×10^{-10}	5.0	0.15–10 mM	1.92·µA·mM^{-1}	0.08	[54]
GCNT/GOx/GAD	+0.44	3.88×10^{-9}	1.08	6.30–20 mM	2.47 µA·mM^{-1}·cm^{-2}	–	[33]
ERCGr–GOx/GCE	–	–	–	2.0–18.0 mM	7 µA·mM^{-1}·cm^{-2}	0.02	[55]
ERGO-SDS-GOx/GCE	–	2.62×10^{-10}	4.1	1.0–8.0 mM	1.13 µA·mM^{-1}·cm^{-2}	0.041	[56]
PPy-rGO-GOx/GCE	+0.9	–	–	0.5–30.0 mM	333 nA·mM^{-1}·cm^{-2}	–	[57]
ERGO-GOx/GCE	−0.44	1.22×10^{-10}	4.8	0.1–27 mM	1.85 µA·mM^{-1}·cm^{-2}	–	[58]
GOD/BCNTs/GCE	–	1.94×10^{-9}	1.56	0.05–0.3 mM	111.6 µA·mM^{-1}·cm^{-2}	0.01	[59]
GOx–GQD/CCE	−0.42	1.8×10^{-9}	1.12	0.005–1.27 mM	85 nA·mM^{-1}·cm^{-2}	0.0017	[60]
GCE/PB/GOx/Au	−0.05	15.23×10^{-9}	2.08	0.08–1.2 mM	1.01 µA·mM^{-1}·cm^{-2}	0.038	**This work**

of GOx on electrode surfaces. For comparison, various glucose sensors with different electrochemical parameters are listed in Table 1.

To determine the detection limit of glucose, the amperometric i-t curve at GCE/PB/GOx/Au electrode in 0.5 M PBS (pH 6.8) with the successive addition of glucose was recorded (Fig. 6h). With the addition of glucose, peak currents gradually increased (Fig. 6h) with a linear relationship with the glucose concentrations in the range from 0 to 1.2 mM. The detection limit was calculated to be about 105 nA mM^{-1} from the slope of the standard curve (I_{pa} (nA) = 0.1 + 0.105c (10^{-6} M), R^2 = 0.9971). The active surface area of the electrode was considered to be 0.1075 cm^2, and the detection sensitivity was about 1011 nA·mM^{-1}·cm^{-2} (Fig. 6h, insert image). For GCE/PB/GOx, the detection sensitivity was calculated to be 32 nA·mM^{-1} from the slope of the standard curve (I_{pa} (nA) = 1.31 + 0.0319c (10^{-6} M), R^2 = 0.9971) and the detection sensitivity was 387 nA·mM^{-1}·cm^{-2} when the active surface area of the electrode (0.0833 cm^2) was considered (**Fig. S16**). The detection limitation (DL) of glucose for the GCE/PB/GOx/Au electrode was calculated to be 38 μM from the expression of DL = 3SD/sensitivity (where SD was the estimated standard deviation for the points used to establish a standard curve and the sensitivity was the slope of the standard curve).

The selectivity of the GCE/PB/GOx/Au electrode for detection glucose was assessed by employing an amperometric i-t curve in 0.05 M PBS (pH 6.8). Interfering substances commonly found in biological fluids, namely ascorbic acid (AA), pyruvic acid (PA), and uric acid (UA), were chosen for evaluation. It was observed that both AA and UA did not impact the detection of glucose, while PA exhibited a slight interference, potentially due to the relatively low applied potential (−0.05 V) of PA (Fig. 6i). This finding strongly suggests that the GCE/PB/GOx/Au electrode exhibits excellent selectivity for glucose detection in biological fluids. Hence, the GCE/PB/GOx/Au glucose sensor holds significant potential for practical applications.

Detection of glutathione (GSH) in cancer patients' blood samples

Organic-inorganic hybrid nanomaterials can achieve similar activity as enzymes [62,63]. Herein, Au@Fmoc-YR was taken to mimic the activity of an oxide enzyme that can oxidize 3,3′,5,5′-tetramethylbenzidine (TMB) to obtain TMB$_{ox}$ with the color change from colorless to blue (652 nm). Meanwhile, TMB$_{ox}$ can be reduced further in the presence of GSH and converted to colorless TMB again [63] (Fig. 7a and **Fig. S17a**). Based on these redox reactions and the color changes, a simple
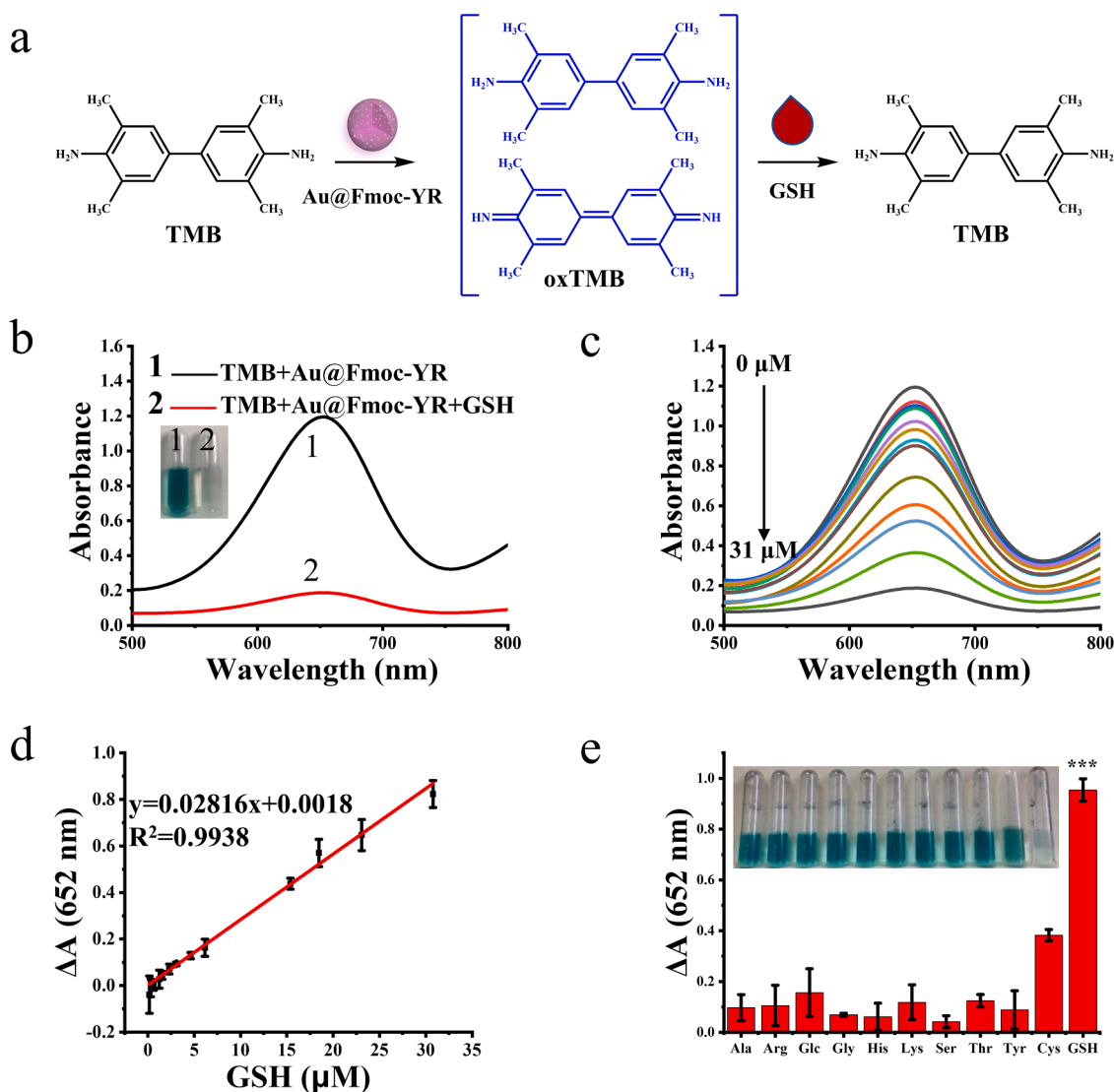
Fig. 7. The detection of GSH. a) TMB-based redox reaction for the detection of GSH. **b)** UV–Vis absorption spectra of TMB in the absence and presence of GSH. **c)** UV–vis absorption spectra of the proposed method in the absence and presence of different concentrations of GSH. **d)** Plots of ΔA (652 nm) with different concentrations of GSH. **e)** Selectivity of the proposed method for GSH against other amino acids or glucose.

colorimetric method of detecting GSH was proposed [64,65]. The absorbance at 652 nm gradually decreased after the addition of GSH (Fig. 7b, c) and the change of absorbance at 652 nm (ΔA) was proportional to the GSH concentrations ($\Delta A_{652} = 0.0018 + 0.02816c$ (μM), $R^2 = 0.9938$, Fig. 7c) with the increase of GSH addition. The linear range of detecting GSH was determined to be 0.15–31 μM and the LOD (limit of detection) was about 0.005 μM (Fig. 7d), which was determined by using the 3σ method and the number of measurements of the blank was 20 times. The selectivity and specificity of the detection method are as important as the detection sensitivity. So different kinds of amino acids including G, S, and H were used in interference experiments (Fig. 7e). Interference factors except Cys-caused only slight absorbance changes at 652 nm. More dipeptides and tripeptides were also used as interference factors for the comparison of GSH (**Fig. S17b**). Only a slight change of absorbance at 652 nm could be observed, indicating good selectivity and specificity of detecting GSH of our method even with the presence of interference factors whether it was amino acids or dipeptides or tripeptides (Fig. 7e and **Fig. S17b**).

To determine the practicability of the method, blood samples of gastric cancer patients were investigated. The blood samples were pretreated with trichloroacetic acid to remove serum proteins and diluted with HAc-NaAc buffer solution [63]. The concentration of GSH in three patients in the blood was 293 ± 39 μM, 300 ± 13 μM, and 622 ± 33 μM, and therefore higher than in the blood sample of healthy individuals [62,63,66]. The abnormal GSH content in blood might be associated with diseases such as tumors, and GSH content might be used as a potential test indicator for early disease screening. It should be noted that few samples were used in this experiment, and more samples need to be tested to obtain meaningful conclusions. A standard addition experiment was performed to reflect the accuracy of test results as different concentrations of GSH were added into the blood samples. Standard recovery rates between 92.6% and 106% in the experiments including three blood samples (**Table S1**) showed good detection accuracy for real samples. The colorimetric method described here helps to determine whether the GSH content in blood was in the normal range through simple color changes, which was meaningful for the rapid screening of samples, and relies on relatively simple testing conditions. The performance of various analytical methods for GSH determination was compared (**Table S2**). The wide detection range and sensitive detection limit compare favorably to the reported previous methods (**Table S2**).

Conclusions

This study presents a method for preparing functional hybrid nanoarchitectures using sequence-dependent dipeptides (Fmoc-YK and Fmoc-YR) and metal ions (Au^{3+}, Ag^+, and Pt^{4+}) under mild and aqueous conditions, without the need for reducing agents or additional chemical modification of peptides. The role of different functional groups of dipeptides and the interaction between the dipeptides and metal ions are described and demonstrated through experimental and molecular dynamics simulation results. These findings indicate that the phenolic hydroxyl of tyrosine is the primary group responsible for reducing metal ions under mild conditions, while positively charged amino or guanidine groups promote the enrichment of Au^{3+} around peptides and facilitate the formation of Au NPs@short peptide nanospheres by electrostatic force. Intriguingly, Ag^+ and Pt^{4+} also exhibit similar behavior to Au^{3+} and can form excellent conductive hybrid peptide nanoarchitectures with good catalytic performance. As proof, Au@Fmoc-YR nanoarchitectures with high surface-to-volume ratio and good dispersibility exhibit enhanced electron transfer on the surface of electrodes, resulting in a significant increase in the rate constant (ks increased from 0.69 to 2.08 s^{-1}). This result demonstrates the potential of these hybrid peptide nanoarchitectures for detecting glucose in different body physiological fluids. Au@Fmoc-YR also shows good catalytic oxidation ability and is used for detecting plasma GSH content in tumor sites of patients with gastric carcinoma, showing good potential application as an early,

metastatic, and recurrent cancer screening tool.

Supporting Information

Supporting Information is available and including: additional experimental details on the catalytic reduction of p-nitrophenol into p-aminophenol, Fig.s S1-S21, and Tables S1-S3.

Declaration of Competing Interest

The authors declare that they have no known competing financial interests or personal relationships that could have appeared to influence the work reported in this paper.

Acknowledgments

Supplementary materials

Supplementary material associated with this article can be found, in the online version, at doi:10.1016/j.supmat.2023.100040.

References

[1] V. Genna, R. Gaspari, M. Dal Peraro, M. De Vivo, Cooperative motion of a key positively charged residue and metal ions for DNA replication catalyzed by human DNA polymerase-η, Nucleic Acids Res 44 (6) (2016) 2827–2836, https://doi.org/10.1093/nar/gkw128.

[2] G. Akanuma, Diverse relationships between metal ions and the ribosome, Biosci., Biotechnol., Biochem 85 (7) (2021) 1582–1593, https://doi.org/10.1093/bbb/zbab070.

[3] R. Yamagami, J.P. Sieg, P.C. Bevilacqua, Functional roles of chelated magnesium ions in RNA folding and function, Biochemistry 60 (31) (2021) 2374–2386, https://doi.org/10.1021/acs.biochem.1c00012.

[4] X. Zhang, Z. Zhu, W. Liu, F. Gao, J. Guo, B. Song, L.P. Lee, F. Zhang, The selective function of quantum biological electron transfer between DNA bases and metal ions in DNA replication, J. Phys. Chem. Lett. 13 (33) (2022) 7779–7787, https://doi.org/10.1021/acs.jpclett.2c01877.

[5] R. Silvestri, V. Nicoli, P. Gangadharannambiar, F. Crea, M.D. Bootman, Calcium signalling pathways in prostate cancer initiation and progression, Nat. Rev. Urol. (2023), https://doi.org/10.1038/s41585-023-00738-x.

[6] K. Krzywoszynska, D. Witkowska, J. Swiatek-Kozlowska, A. Szebesczyk, H. Kozlowski, General aspects of metal ions as signaling agents in health and disease, Biomolecules 10 (10) (2020) 1417, https://doi.org/10.3390/biom10101417.

[7] X. Lv, J. Huang, J. Min, H. Wang, Y. Xu, Z. Zhang, X. Zhou, J. Wang, Z. Liu, H. Zhao, Multi-signaling pathway activation by pH responsive manganese particles for enhanced vaccination, J. Controlled Rel. 357 (2023) 109–119, https://doi.org/10.1016/j.jconrel.2023.01.078.

[8] S. Solier, S. Muller, T. Caneque, A. Versini, A. Mansart, F. Sindikubwabo, L. Baron, L. Emam, P. Gestraud, G.D. Pantos, V. Gandon, C. Gaillet, T.D. Wu, F. Dingli, D. Loew, S. Baulande, S. Durand, V. Sencio, C. Robil, F. Trottein, D. Pericat, E. Naser, C. Cougoule, E. Meunier, A.L. Begue, H. Salmon, N. Manel, A. Puisieux, S. Watson, M.A. Dawson, N. Servant, G. Kroemer, D. Annane, R. Rodriguez, A druggable copper-signalling pathway that drives inflammation, Nature 617 (7960) (2023) 386–394, https://doi.org/10.1038/s41586-023-06017-4.

[9] S. Bai, Y. Lan, S. Fu, H. Cheng, Z. Lu, G. Liu, Connecting calcium-based nanomaterials and cancer: from diagnosis to therapy, Nano-Micro Lett. 14 (1) (2022) 145, https://doi.org/10.1007/s40820-022-00894-6.

[10] H. Song, Q. Su, Y. Nie, C. Zhang, P. Huang, S. Shi, Q. Liu, W. Wang, Supramolecular assembly of a trivalent peptide hydrogel vaccine for cancer immunotherapy, Acta Biomater 158 (2023) 535–546, https://doi.org/10.1016/j.actbio.2022.12.070.

[11] Z. Ren, S. Sun, R. Sun, G. Cui, L. Hong, B. Rao, A. Li, Z. Yu, Q. Kan, Z. Mao, A metal-polyphenol-coordinated nanomedicine for synergistic cascade cancer chemotherapy and chemodynamy therapy, Adv. Mater. 32 (6) (2020) 1906024, https://doi.org/10.1002/adma.201906024.

[12] F. Cao, L. Jin, Y. Gao, Y. Ding, H. Wen, Z. Qian, C. Zhang, L. Hong, H. Yang, J. Zhang, Z. Tong, W. Wang, X. Chen, Z. Mao, Artificial-enzymes-armed

bifidobacterium longum probiotics for alleviating intestinal inflammation and microbiota dysbiosis, Nat. Nanotechnol. 18 (6) (2023) 617–627, https://doi.org/10.1038/s41565-023-01346-x.

[13] X. Ma, Y. Liu, S. Li, K. Ogino, R. Xing, X. Yan, Multicomponent coassembled nanodrugs based on ovalbumin, pheophorbide a and Zn^{2+} for in vitro photodynamic therapy, Supramolecular Mater. 1 (2022), 100010, https://doi.org/10.1016/j.supmat.2022.100010.

[14] G. Fichman, E. Gazit, Self-assembly of short peptides to form hydrogels: design of building blocks, physical properties and technological applications, Acta Biomater. 10 (4) (2014) 1671–1682, https://doi.org/10.1016/j.actbio.2013.08.013.

[15] T. Yuan, Y. Xu, J. Fei, H. Xue, X. Li, C. Wang, G. Fytas, J. Li, The ultrafast assembly of a dipeptide supramolecular organogel and its phase transition from gel to crystal, Angew. Chem., Int. Ed. 58 (32) (2019) 11072–11077, https://doi.org/10.1002/anie.201903829.

[16] R. Teng, Y. Yang, Z. Zhang, K. Yang, M. Sun, C. Li, Z. Fan, J. Du, In situ enzyme-induced self-assembly of antimicrobial-antioxidative peptides to promote wound healing, Adv. Funct. Mater. (2023), 2214454, https://doi.org/10.1002/adfm.202214454.

[17] S.H. Hiew, Y. Lu, H. Han, R.A. Goncalves, S.R. Alfarano, R. Mezzenga, A.N. Parikh, Y. Mu, A. Miserez, Modulation of mechanical properties of short bioinspired peptide materials by single amino-acid mutations, J. Am. Chem. Soc. 145 (6) (2023) 3382–3393, https://doi.org/10.1021/jacs.2c09853.

[18] S. Yang, M. Wang, T. Wang, M. Sun, H. Huang, X. Shi, S. Duan, Y. Wu, J. Zhu, F. Liu, Self-assembled short peptides: recent advances and strategies for potential pharmaceutical applications, Mater. Today Bio (2023), 100644, https://doi.org/10.1016/j.mtbio.2023.100644.

[19] Y. Zhou, Q. Li, Y. Wu, X. Li, Y. Zhou, Z. Wang, H. Liang, F. Ding, S. Hong, N. F. Steinmetz, H. Cai, Molecularly stimuli-responsive self-assembled peptide nanoparticles for targeted imaging and therapy, ACS Nano 17 (9) (2023) 8004–8025, https://doi.org/10.1021/acsnano.3c01452.

[20] D. Wang, N. Zhang, T. Yang, Y. Zhang, X. Jing, Y. Zhou, J. Long, L. Meng, Amino acids and doxorubicin as building blocks for metal ion-driven self-assembly of biodegradable polyprodrugs for tumor theranostics, Acta Biomater 147 (2022) 245–257, https://doi.org/10.1016/j.actbio.2022.04.034.

[21] M. Abbas, A. Atiq, R. Xing, X. Yan, Silver-incorporating peptide and protein supramolecular nanomaterials for biomedical applications, J. Mater. Chem. B 9 (22) (2021) 4444–4458, https://doi.org/10.1039/D1TB00025J.

[22] C. Yuan, A. Levin, W. Chen, R. Xing, Q. Zou, T.W. Herling, P.K. Challa, T.P. J. Knowles, X. Yan, Nucleation and growth of amino acid and peptide supramolecular polymers through liquid-liquid phase separation, Angew. Chem., Int. Ed. 58 (50) (2019) 18116–18123, https://doi.org/10.1002/anie.201911782.

[23] A.D. Merg, J.C. Boatz, A. Mandal, G. Zhao, S. Mokashi-Punekar, C. Liu, X. Wang, P. Zhang, P.C.A. van der Wel, N.L. Rosi, Peptide-directed assembly of single-helical gold nanoparticle superstructures exhibiting intense chiroptical activity, J. Am. Chem. Soc. 138 (41) (2016) 13655–13663, https://doi.org/10.1021/jacs.6b07322.

[24] S. Mokashi-Punekar, A.D. Merg, N.L. Rosi, Systematic adjustment of pitch and particle dimensions within a family of chiral plasmonic gold nanoparticle single helices, J. Am. Chem. Soc. 139 (42) (2017) 15043–15048, https://doi.org/10.1021/jacs.7b07143.

[25] S. Mokashi-Punekar, S.C. Brooks, C.D. Hogan, N.L. Rosi, Leveraging peptide sequence modification to promote assembly of chiral helical gold nanoparticle superstructures, Biochemistry 60 (13) (2021) 1044–1049, https://doi.org/10.1021/acs.biochem.0c00361.

[26] S.C. Brooks, R. Jin, V.C. Zerbach, Y. Zhang, T.R. Walsh, N.L. Rosi, Single amino acid modifications for controlling the helicity of peptide-based chiral gold nanoparticle superstructures, J. Am. Chem. Soc. 145 (11) (2023) 6546–6553, https://doi.org/10.1021/jacs.3c00827.

[27] C. Pigliacelli, K.B. Sanjeeva, A.Pizzi Nonappa, A. Gori, F.B. Bombelli, P. Metrangolo, In situ generation of chiroptically-active gold-peptide superstructures promoted by iodination, ACS Nano 13 (2) (2019) 2158–2166, https://doi.org/10.1021/acsnano.8b08805.

[28] Y. Gong, X. Chen, Y. Lu, W. Yang, Self-assembled dipeptide-gold nanoparticle hybrid spheres for highly sensitive amperometric hydrogen peroxide biosensors, Biosens. Bioelectron. 66 (2015) 392–398, https://doi.org/10.1016/j.bios.2014.11.029.

[29] L. Lv, X. Han, X. Wu, C. Li, The synthesis of high-aspect-ratio Au microwires with a biomolecule for electrochemical sensing, Chem. Commun. 56 (5) (2020) 743–746, https://doi.org/10.1039/c9cc06523g.

[30] X. Zhang, X. Chen, Y. Zhao, Nanozymes: versatile platforms for cancer diagnosis and therapy, Nano-Micro Lett. 14 (1) (2022) 95, https://doi.org/10.1007/s40820-022-00828-2.

[31] G. Siest, A. Nicolas, M. Wellman, P. Leroy, R. Gueguen, F. Michelet, Blood and plasma glutathione measured in healthy subjects by HPLC: relation to sex, aging, biological variables, and life habits, Clin. Chem. 41 (10) (1995) 1509–1517, https://doi.org/10.1093/clinchem/41.10.1509.

[32] W. Gao, S. Emaminejad, H.Y.Y. Nyein, S. Challa, K. Chen, A. Peck, H.M. Fahad, H. Ota, H. Shiraki, D. Kiriya, D.-H. Lien, G.A. Brooks, R.W. Davis, A. Javey, Fully integrated wearable sensor arrays for multiplexed in situ perspiration analysis, Nature 529 (7587) (2016) 509–514, https://doi.org/10.1038/nature16521.

[33] A.P. Periasamy, Y.-J. Chang, S.-M. Chen, Amperometric glucose sensor based on glucose oxidase immobilized on gelatin-multiwalled carbon nanotube modified glassy carbon electrode, Bioelectrochemistry 80 (2) (2011) 114–120, https://doi.org/10.1016/j.bioelechem.2010.06.009.

[34] Y. Wu, Y. Kong, K. Lu, M. Lv, Y. Ye, Y. Zhao, An easy fabrication of glucose oxidase-dipeptide-reduced graphene oxide nanocomposite for glucose sensing, Mater. Res. Bull. 94 (2017) 378–384, https://doi.org/10.1016/j.materresbull.2017.06.001.

[35] V. Mani, B. Devadas, S.-M. Chen, Direct electrochemistry of glucose oxidase at electrochemically reduced graphene oxide-multiwalled carbon nanotubes hybrid material modified electrode for glucose biosensor, Biosens. Bioelectron. 41 (2013) 309–315, https://doi.org/10.1016/j.bios.2012.08.045.

[36] S. Palanisamy, C. Karuppiah, S.-M. Chen, R. Emmanuel, P. Muthukrishnan, P. Prakash, Direct electrochemistry of myoglobin at silver nanoparticles/ myoglobin biocomposite: application for hydrogen peroxide sensing, Sensors Actuators B: Chem 202 (2014) 177–184, https://doi.org/10.1016/j.snb.2014.05.069.

[37] X. Liu, Z. Nan, Y. Qiu, L. Zheng, X. Lu, Hydrophobic ionic liquid immoblizing cholesterol oxidase on the electrodeposited prussian blue on glassy carbon electrode for detection of cholesterol, Electrochim. Acta 90 (2013) 203–209, https://doi.org/10.1016/j.electacta.2012.11.119.

[38] T. Maruyama, Y. Fujimoto, T. Maekawa, Synthesis of gold nanoparticles using various amino acids, J. Colloid Interface Sci. 447 (2015) 254–257, https://doi.org/10.1016/j.jcis.2014.12.046.

[39] K.-I. Min, S.-W. Lee, E.-H. Lee, Y.-S. Lee, H. Yi, D.-P. Kim, Facile nondestructive assembly of tyrosine-rich peptide nanofibers as a biological glue for multicomponent-based nanoelectrode applications, Adv. Funct. Mater. 28 (11) (2018), 1705729, https://doi.org/10.1002/adfm.201705729.

[40] K. Wang, Z. Li, C. Wang, S. Zhang, W. Cui, Y. Xu, J. Zhao, H. Xue, J. Li, Assembled cationic dipeptide-gold nanoparticle hybrid microspheres for electrochemical biosensors with enhanced sensitivity, J. Colloid Interface Sci. 557 (2019) 628–634, https://doi.org/10.1016/j.jcis.2019.09.033.

[41] K.-I. Min, G. Yun, Y. Jang, K.-R. Kim, Y.H. Ko, H.-S. Jang, Y.-S. Lee, K. Kim, D.-P. Kim, Covalent self-assembly and one-step photocrosslinking of tyrosine-rich oligopeptides to form diverse nanostructures, Angew. Chem., Int. Ed. 55 (24) (2016) 6925–6928, https://doi.org/10.1002/anie.201601675.

[42] P. Ren, J. Li, L. Zhao, A. Wang, M. Wang, J. Li, H. Jian, X. Li, X. Yan, S. Bai, Dipeptide self-assembled hydrogels with shear-thinning and instantaneous self-healing properties determined by peptide sequences, ACS Appl. Mater. Interfaces. 12 (19) (2020) 21433–21440, https://doi.org/10.1021/acsami.0c03038.

[43] H. Jian, M. Wang, Q. Dong, J. Li, A. Wang, X. Li, P. Ren, S. Bai, Dipeptide self-assembled hydrogels with tunable mechanical properties and degradability for 3D bioprinting, ACS Appl. Mater. Interfaces. 11 (50) (2019) 46419–46426, https://doi.org/10.1021/acsami.9b13905.

[44] M. Wang, Q. Zhang, H. Jian, S. Liu, J. Li, A. Wang, Q. Dong, P. Ren, X. Li, S. Bai, Role of thermolysin in catalytic-controlled self-assembly of Fmoc-dipeptides, CCS Chem. 2 (4) (2020) 317–328, https://doi.org/10.31635/ccschem.020.201900116.

[45] K.-I. Min, D.-H. Kim, H.-J. Lee, L. Lin, D.-P. Kim, Direct synthesis of a covalently self-assembled peptide nanogel from a tyrosine-rich peptide monomer and its biomineralized hybrids, Angew. Chem., Int. Ed. 57 (20) (2018) 5630–5634, https://doi.org/10.1002/anie.201713261.

[46] F. Kang, X. Qu, P.J.J. Alvarez, D. Zhu, Extracellular saccharide-mediated reduction of Au^{3+} to gold nanoparticles: new insights for heavy metals biomineralization on microbial surfaces, Environ. Sci. Technol. 51 (5) (2017) 2776–2785, https://doi.org/10.1021/acs.est.6b05930.

[47] S. He, J. Shi, E. Walid, H. Zhang, Y. Ma, S.J. Xue, Reverse micellar extraction of lectin from black turtle bean (phaseolus vulgaris): optimisation of extraction conditions by response surface methodology, Food Chem. 166 (2015) 93–100, https://doi.org/10.1016/j.foodchem.2014.05.156.

[48] M. Carbonaro, A. Nucara, Secondary structure of food proteins by fourier transform spectroscopy in the Mid-infrared region, Amino Acids 38 (3) (2009) 679–690, https://doi.org/10.1007/s00726-009-0274-3.

[49] H.-S. Shin, J.-Y. Hong, S. Huh, 2-thiopheneacetic acid directed synthesis of Au nanorosette as an SERS-active substrate, ACS Appl. Mater. Interfaces. 5 (4) (2013) 1429–1435, https://doi.org/10.1021/am302865b.

[50] N. Lee, H.-S. Jang, M. Lee, Y.-O. Kim, H.-J. Cho, D.H. Jeong, D.-S. Shin, Y.-S. Lee, D.-W. Lee, S.-M. Lee, Au ion-mediated self-assembled tyrosine-rich peptide nanostructure embedded with gold nanoparticle satellites, J. Ind. Eng. Chem. 64 (2018) 461–466, https://doi.org/10.1016/j.jiec.2018.04.007.

[51] Y.L. Yao, K.K. Shiu, Direct electrochemistry of glucose oxidase at carbon nanotube-gold colloid modified electrode with poly(diallyldimethylammonium chloride) coating, Electroanalysis 20 (14) (2008) 1542–1548, https://doi.org/10.1002/elan.200804209.

[52] Y. Liu, S. Wu, H. Ju, L. Xu, Amperometric glucose biosensing of gold nanoparticles and carbon nanotube multilayer membranes, Electroanalysis 19 (9) (2007) 986–992, https://doi.org/10.1002/elan.200603814.

[53] Y.-L. Yao, K.-K. Shiu, Low potential detection of glucose at carbon nanotube modified glassy carbon electrode with electropolymerized poly(toluidine blue O) film, Electrochim. Acta 53 (2) (2007) 278–284, https://doi.org/10.1016/j.electacta.2007.04.007.

[54] Q. Sheng, K. Luo, L. Li, J. Zheng, Direct electrochemistry of glucose oxidase immobilized on $NdPO_4$ nanoparticles/chitosan composite film on glassy carbon electrodes and its biosensing application, Bioelectrochemistry 74 (2) (2009) 246–253, https://doi.org/10.1016/j.bioelechem.2008.08.007.

[55] B. Liang, L. Fang, G. Yang, Y. Hu, X. Guo, X. Ye, Direct electron transfer glucose biosensor based on glucose oxidase self-assembled on electrochemically reduced carboxyl graphene, Biosens. Bioelectron. 43 (2013) 131–136, https://doi.org/10.1016/j.bios.2012.11.040.

[56] M. Shamsipur, M. Amouzadeh Tabrizi, Achieving direct electrochemistry of glucose oxidase by one step electrochemical reduction of graphene oxide and its use in glucose sensing, Mater. Sci. Eng., C 45 (2014) 103–108, https://doi.org/10.1016/j.msec.2014.09.002.

[57] E.-R. Lin, C.-J. Chiu, Y.-C. Tsaiz, One-step electrochemical synthesis of polypyrrole-graphene-glucose oxidase nanobiocomposite for glucose sensing, J. Electrochem. Soc. 161 (12) (2014) B243–B247, https://doi.org/10.1149/2.0091412jes.

[58] B. Unnikrishnan, S. Palanisamy, S.-M. Chen, A simple electrochemical approach to fabricate a glucose biosensor based on graphene-glucose oxidase biocomposite, Biosens. Bioelectron. 39 (1) (2013) 70–75, https://doi.org/10.1016/j.bios.2012.06.045.

[59] C. Deng, J. Chen, X. Chen, C. Xiao, L. Nie, S. Yao, Direct electrochemistry of glucose oxidase and biosensing for glucose based on boron-doped carbon nanotubes modified electrode, Biosens. Bioelectron. 23 (8) (2008) 1272–1277, https://doi.org/10.1016/j.bios.2007.11.009.

[60] H. Razmi, R. Mohammad-Rezaei, Graphene quantum dots as a new substrate for immobilization and direct electrochemistry of glucose oxidase: application to sensitive glucose determination, Biosens. Bioelectron. 41 (2013) 498–504, https://doi.org/10.1016/j.bios.2012.09.009.

[61] J.-Z. Xu, J.-J. Zhu, Q. Wu, Z. Hu, H.-Y. Chen, Direct electron transfer between glucose oxidase and multi-walled carbon nanotubes, Chin. J. Chem. 21 (2003) 1088–1091, https://doi.org/10.1002/cjoc.20030210822.

[62] X. Liu, Q. Wang, Y. Zhang, L. Zhang, Y. Su, Y. Lv, Colorimetric detection of glutathione in human blood serum based on the reduction of oxidized TMB, New J. Chem. 37 (7) (2013) 2174, https://doi.org/10.1039/c3nj40897c.

[63] Q. Zhong, Y. Chen, A. Su, Y. Wang, Synthesis of catalytically active carbon quantum dots and its application for colorimetric detection of glutathione, Sensors Actuators B: Chem 273 (2018) 1098–1102, https://doi.org/10.1016/j.snb.2018.07.026.

[64] B. Navyatha, S. Singh, S. Nara, Auperoxidase nanozymes: promises and applications in biosensing, Biosens. Bioelectron. 175 (2021) 112882, https://doi.org/10.1016/j.bios.2020.112882.

[65] L. Tan, Y. Zhang, H. Qiang, Y. Li, J. Sun, L. Hu, Z. Chen, A sensitive Hg(II) colorimetric sensor based on synergistic catalytic effect of gold nanoparticles and Hg, Sensors Actuators B: Chem 229 (2016) 686–691, https://doi.org/10.1016/j.snb.2016.02.037.

[66] I. Rahman, A. Kode, S.K. Biswas, Assay for quantitative determination of glutathione and glutathione disulfide levels using enzymatic recycling method, Nat. Protoc. 1 (6) (2007) 3159–3165, https://doi.org/10.1038/nprot.2006.378.